Modified Phase-Offset-Driven Lissajous Scanning Endomicroscopy With a Polyimide-Film-Based Frequency Separator

Jintaek Im, Yeonhee Chang, *Student Member, IEEE*, and Cheol Song, *Member, IEEE*

***Abstract*—This article presents a Lissajous scanning confocal endomicroscopy comprising an easily manufacturable thin polyimide (PI) film and modified phase-offset-driven scanning. The Lissajous scanning confocal probe has a piezoelectric tube actuator and the PI film-attached fiber cantilever designed to resonate with the lever mechanism. Data from a finite element analysis and experiments are used to optimize the dimensions of the PI film, which produces a frequency separation and field of view of $195\ \mathrm{Hz}$ and $180\ \mu\mathrm{m} \times 180\ \mu\mathrm{m}$, respectively, at driving voltages less than $30\ \mathrm{V}_{pp}$. The best combination of decimal frequencies with optimized driving phase offsets is determined to achieve a scanning density (SD) exceeding 80% consistently with an imaging speed of $8\ \mathrm{Hz}$. By analyzing the Lissajous patterns at different decimal frequency combinations via time-delay analysis, it is possible to find more diverse combinations that meet the SD criterion. When the scanning patterns deviate from the desired paths, the proposed modified phase-offset-driven method is applied to maintain the best scanning pattern. The USAF 1951 test pattern, several plants, and rat gastrointestinal tract were imaged successfully using the confocal endomicroscopic system with the PI film and modified phase-offset-driven scanning.**

***Index Terms*—Confocal endomicroscopic system, lissajous scanning, modified phase-offset-driven method, polyimide (PI) film.**

Manuscript received 12 May 2021; revised 15 September 2021, 23 November 2021, and 31 January 2022; accepted 16 March 2022. Date of publication 27 April 2022; date of current version 14 December 2022. Recommended by Technical Editor Y. K. Yong and Senior Editor Q. Zou. This work was supported in part by the Ministry of Trade Industry & Energy (MOTIE, Korea), Ministry of Science & ICT (MSIT, Korea), and in part by the Ministry of Health & Welfare (MOHW, Korea) under Technology Development Program for AI-Bio-Robot-Medicine Convergence under Grant 20001533, and in part by the DGIST R&D Program of the Ministry of Science and ICT under Grant 22-RT-01. *(Corresponding author: Cheol Song.)*

The authors are with the Department of Robotics and Mechatronics Engineering, Daegu Gyeongbuk Institute of Science and Technology, Daegu, South Korea (e-mail: wlsehd23@dgist.ac.kr; nyonuimon@dgist.ac.kr; csong@dgist.ac.kr).

This work involved animals in its research. Approval of all ethical and experimental procedures and protocols was granted by the Animal Experiment Ethics Committee of Doegu Gyeongbuk Institute of Science and Technology, DGIST-IACVC-21042801-0001.

This article has supplementary material provided by the authors and color versions of one or more figures available at https://doi.org/10.1109/TMECH.2022.3166453.

Digital Object Identifier 10.1109/TMECH.2022.3166453

I. Introduction

Real-time visualization of microscopic objects is required in several fields for manufacturing, micromanipulation, vision-based control, and biomedical applications, among others [1]–[5]. Images can be obtained by sequentially illuminating samples pointwise and recording the reflected light from all scanned points within the field of view (FOV) [6]. Recent studies have used several microelectromechanical systems or piezoelectric (PZT) tube actuators to maneuver the scanning cantilever in both benchtop-type scanning probe microscopies such as atomic force microscopy [7], [8] and probe-type endomicroscopy [9], [10]. In particular, the endomicroscopic optical probe requires a miniature actuator to be integrated within a compact tubular package (probe) and operated with low driving voltages $< 42\ \mathrm{V}_{\mathrm{ac}}$ for medical endoscopic applications [11]. An optical fiber is used as the scanning cantilever to implement the miniaturized probe, and the PZT tube actuator vibrates the fiber cantilever by resonance to achieve a wide FOV with a low driving voltage [12], [13].

Two sinusoidal driving voltages are commonly used to actuate the resonant scanner, and the waveforms determine the scanning patterns. If the driving frequencies of the two orthogonal scanning axes are identical, a spiral [7] or cycloid [8] scanning pattern is considered. However, raster [14] or Lissajous [15] scanning methods can be chosen for two different scanning frequencies. For a resonant fiber scanning system using the PZT tube actuator, it is desirable to separate the resonant frequencies to preclude parasitic resonances due to the mechanical coupling of the PZT tube actuator [16]. The parasitic resonance inhibits the fiber cantilever from achieving a clear and precise line scanning and orthogonality of two scanning axes [17]. In addition, raster scanning necessitates a non-resonant axis to which a high driving voltage should be applied [14]. Lissajous scanning can be achieved with two different resonant frequencies to avoid parasitic resonance and provide high imaging speeds with uniform illuminations [18]. Hence, Lissajous scanning is chosen as the preferred method in this study.

The frequency [19], [20] and phase [21], [22] combinations are the crucial parameters in Lissajous scanning. In particular, the scanning density (SD) is mainly dependent on the ratio of driving frequencies. A scanner with a wide resonant bandwidth $\sim$ 100 Hz has several integer frequency combinations with large greatest-common-factors to achieve repeated

high-SD images rapidly [19]. The greatest common factor of two integer frequencies and their quotients are related to the imaging speed and SD, respectively; thus, there is a tradeoff relationship between imaging speed and SD [20]. However, the miniature PZT scanner often has a narrow resonant bandwidth of the order of several hertz [23], [24] to $\sim$ 1 Hz [25]; hence, it can be challenging to find the best integer frequency combinations in such cases.

The integer driving frequency can be chosen near the resonant peak for such narrow-bandwidth scanners. However, the high-Q-factor scanner does not allow a sufficient FOV at the semi-resonant frequencies [17], [25]. As an alternative strategy, frequency combinations with decimal numbers can be considered. If their frequency ratio is not a rational number, it results in a non-repeating Lissajous pattern [26]. In the nonrepeating scanning pattern, the SD of each acquired image changes continuously. This variation in SD sometimes produces poorly sampled images, and a temporal averaging using the previously sampled image has been used to increase both SD and the imaging speed [27], [28]. However, the temporal averaging method is susceptible to motion blurs. Moreover, all acquired images have spatially enough SD at a fast imaging speed. To find the desired non-repeating Lissajous pattern that can continuously provide high SDs, we analyzed the frequency combination and the time-delay difference affecting the SDs.

Although the predetermined condition for the desired Lissajous pattern is found, the image matching phases (mapping phases) should be modulated to compensate for the phase difference between the driving signal and actual beam path [29]. The phase difference between the driving signal and actual beam position result from the resonant phase shifts ranging from $-\pi$ to 0 [30]. Image matching is the procedure used to identify the actual phase, and hardware- or software-based solutions have been suggested for image matching. Hardware-based solutions involve additional parts for closed-loop control, such as position-sensitive detectors [24] or reference apertures [30] with integrated circuits [31], [32]; however, they cause more complexity and increased dimensionality in the probe housing design [24], which should be avoided for endomicroscopic applications. Contrarily, software-based solutions use only the acquired images to identify the actual phase [29], [33] without sensor feedback; phase identification can be achieved by modulating the mapping phases via user interface either manually or automatically while monitoring the acquired images. Hence, software-based solutions have advantages in terms of cost and simplicity of design of the endomicroscopic probe design.

In the present work, a probe-type Lissajous scanning confocal endomicroscopy is presented using the modified phase-offset-driven method. Confocal endomicroscopic systems can help visualize *in-vivo* histological images with a relatively simple setup and the fluorescent agent "fluorescein," approved by the Food and Drug Administration [34]. The presented system uses the best combinations of both decimal frequencies and phases to achieve consistently high SDs images, analyzed by MATLAB software within the narrow frequency bandwidth. For the analyses, the SD criterion is set to $> 80\%$, which has been previously used as a threshold for real-time Lissajous scanning [16], [20]. In addition, the modified phase-offset-driven method is applied to maintain the best Lissajous pattern by compensating for the phase deviations from the optimal values. We demonstrate by both MATLAB simulations and experiments that the modified phase offset-driven method can preserve the best scanning patterns, even if the actual phases deviate from the optimal values.

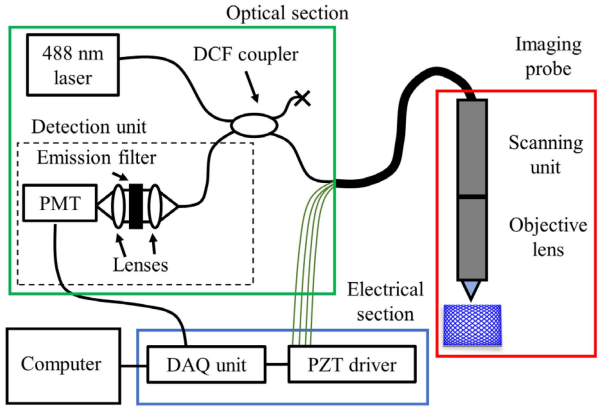

Fig. 1. System configuration: optical section, electrical section, a computer, and an imaging probe.

In the Lissajous scanner, an asymmetric configuration of the optical fiber [17] or an additional attachable part [16], [24] has been introduced to divide the resonant frequencies of the first and second modes; the higher modes are generally not concerned with a two-dimensional resonant fiber scanner using the PZT tube actuator. We select the polyimide (PI) film as a frequency separator because it offers several advantages, such as low cost, good mechanical strength, and high dimensional stability, which are promising for frequency separation in a resonant fiber-scanning system [35]. Moreover, commercially available PI films can be quickly adopted with the desired dimensions before being attached to the fiber cantilever. By attaching the PI film to the fiber cantilever, the PI-film-attached fiber cantilever (PIF-FC) can resonate with the lever mechanism. Once the optimal lever length is determined, the highest deflection of the fiber cantilever is achieved with a narrow resonant frequency bandwidth.

The rest of this article is organized as follows. Section II presents the implementation of the PIF-FC Lissajous confocal endomicroscopic system. Section III describes the modified phase-offset-driven method. The images of USAF 1951 test pattern, several plants, and a rat gastrointestinal tract are successfully acquired using our system. Finally, Section V concludes this article.

II. PIF-FC Lissajous Confocal Imaging System

A. System Configuration

The configuration of the proposed confocal endomicroscopic system is shown in Fig. 1. The system consists of the optical section, electrical section, a computer, and an imaging probe. The optical section constitutes a 488 nm laser (OBIS

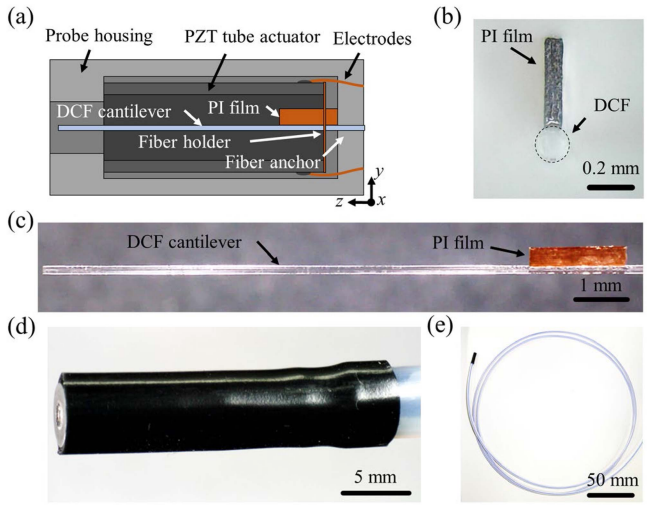

Fig. 2. (a) Inner structure of the scanning unit. (b) and (c) Images of the PIF-FC from the xy and yz planes, respectively. (d) and (e) Images of the implemented imaging probe.

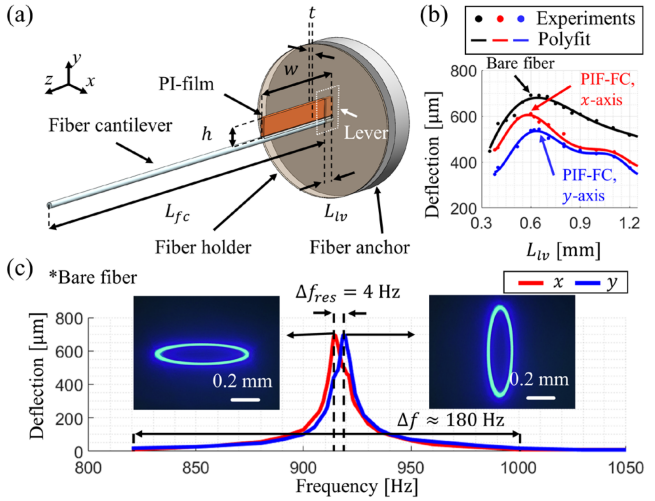

Fig. 3. (a) Schematic and parameters of the scanning unit. (b) Deflection results of a bare fiber cantilever and PIF-FC for the lever length. (c) Frequency responses of the bare fiber along the scanning axes.

488 nm, Coherent, Inc., USA), a double-clad fiber (DCF) coupler (DC530SEFA, Thorlabs, USA), and a detection unit comprising one collimation lens, one emission filter, one focusing lens, and a photomultiplier tube (PMT, R6355, Hamamatsu Photonics K.K., Japan). The emission filter is placed in front of the collimation lens to transmit the excited fluorescent light at wavelengths of 520–530 nm. Then, light is illuminated on the PMT through the focusing lens. The intensity of the collected light is amplified and recorded with a computer through a data acquisition (DAQ) unit (USB-6003 and PCIe-6374, National Instruments, USA) in the electrical section. The electrical section also includes a multichannel PZT driver (E-413.60, Pi Ceramic, Germany) to operate the PZT tube actuator. The DAQ unit generates two sinusoidal waveforms to drive the PZT tube actuator, and these are each amplified by a factor of 25 in the PZT driver. The driving voltages are synchronized with signals from the PMT using a common clock signal of 3.2 MHz. Then, the 8-bit images are created with the mapping waveform and recorded intensities. The imaging probe consists of the scanning unit and objective lens, as indicated by the red-colored box in Fig. 1.

Fig. 2(a) shows the inner structure of the scanning unit; a DCF (DCF530S, Caster Optics, Canada) is used as the scanning optical fiber, and a commercial PZT tube actuator (Pi ceramic, Germany) with an outer diameter of 3.2 mm and thickness of 0.5 mm is precisely manufactured to a length of 8.5 mm. The end of the PZT tube actuator close to the fiber tip is fixed at the probe housing using epoxy resin. In addition, four thin electrodes are attached to each quadrant surface of the PZT tube actuator. A lever mechanism can be introduced to increase the deflection of the fiber cantilever. The reverse-mounted configuration has been used to implement the lever mechanism with the PZT tube actuator in literature [14], [23]. Here, we fixed a part of the fiber cantilever at a fiber anchor, and the PZT tube actuator encloses the remaining part. Then, the fiber cantilever is deflected by the fiber holder coaxially connecting the fiber cantilever and PZT tube actuator.

The PI film is then attached perpendicular to the fiber cantilever using UV-curable epoxy to fabricate the PIF-FC. Then, the PIF-FC is passed through the fiber holder made of rigid polyamide-imides of a thickness of 0.05 mm. A hole is engraved at the center of the fiber holder to fit the PIF-FC; thus, it is easy to insert the PIF-FC, and the fiber holder can effectively transmit the load generated by the PZT tube actuator. The fiber anchor works as a fulcrum, and the PZT tube actuator load is exerted on the fiber cantilever via the fiber holder. The manufactured scanning unit's outer diameter and rigid length are 4.4 mm and 12 mm, respectively.

Fig. 2(b) and (c) is the image of the PIF-FC along the xy and yz planes, respectively. The PI film has uniform thickness and is carefully manufactured to have the desired dimensions. The assembled imaging probe is wrapped in a nonconductive hypodermic tube, as shown in Fig. 2(d). Then, the fiber and electrodes are enclosed within a polytetrafluoroethylene tube for protection from excessive bending, as shown in Fig. 2(e).

B. Optimization of Film Dimension

Fig. 3(a) shows the schematic and parameters of the scanning unit. First, the variable L_{fc} represents the length of the fiber cantilever, which is defined as the distance from the fiber holder to the fiber tip and is set to 10.25 mm. L_{fc} is determined to have a predetermined offset of 0.5 mm from the objective lens. L_{lv} is the length of the lever, which refers to the part of the fiber cantilever between the fiber anchor and fiber holder, as indicated by the white dotted box. The PI film has three defining parameters: w, h, and t, representing the width, height, and thickness. w and h can be adjusted, whereas t is fixed at 0.08 mm, as it is the thickness of a commercially available PI film we used.

According to the lever and elastic deformation mechanism, an optimal lever length produces the highest deflection of the fiber cantilever [36]. In this study, the optimal L_{lv} is determined experimentally using a bare fiber cantilever and PIF-FC, as

shown in Fig. 3(b). A driving voltage amplitude of 25 V_{pp} is applied for both cases. L_{fc} is fixed to maintain the distance from the fiber tip to the first surface of the objective lens, and the deflections of the fiber tip at its resonant frequency (f_{res}) are measured by varying L_{lv} from 0.3 to 1.2 mm. The maximum deflection of 0.69 mm is measured at $L_{lv} = 0.6$ mm in the bare fiber. The bare fiber is symmetric along the z-axis, so it has almost similar flexural rigidities along the x- and y-axes.

On the other hand, PIF-FC has two different flexural rigidities along the scanning axes, which affects the optimal lever length [36]. The x-axis deflection is not affected much by the attachment of the PI film owing to its low thickness; hence, the same optimal L_{lv} of 0.6 mm as the bare fiber is achieved. The PI film attachment mainly affects the flexural rigidity along the y-axis, resulting in a shift of the optimal L_{lv} from 0.6 to 0.65 mm for a PI film with w and h of 1.7 and 0.35 mm, respectively. This shift can be varied in different dimensions of the PI film. However, the shift amount of the optimal L_{lv} can be confined by setting the upper boundary of the y-axis stiffness. We decided to use the L_{lv} of 0.6 mm, which is also valid for the PIF-FC. Fig. 3(c) depicts the frequency response of the bare fiber cantilever along each scanning axis for the same L_{fc} and L_{lv} of 0.6 mm. A slight frequency separation, Δf_{res}, of 4 Hz is observed owing to the inherent asymmetricities of the components in the scanning unit.

However, this difference is not large enough to exclude resonance by the parasitic motion of the PZT along each axis; thus, the scanning patterns of the bare fiber have elliptical shapes. To determine the required frequency difference, Δf, to avoid parasitic resonance, the frequency boundaries are selected such that the fiber deflection cannot be further detected by the digital microscope (INSPEX 3, Ash Technologies, Ireland); thus, a Δf of 180 Hz is decided so that Δf_{res} is larger than 180 Hz.

To separate the resonant frequencies, it is important to identify the tendency of Δf_{res} with respect to the dimensions of the attached PI film. The resonant frequency of the bare fiber cantilever can be expressed as $f_{res} = \frac{C^2}{2\pi {L_{fc}}^2}\sqrt{\frac{EI}{\rho A}}$, where EI is the flexural rigidity, ρ is the density, A is the cross-sectional area of the PIF-FC, and C is a mode number constant [37]. EI along the x-axis is always larger than y-axis in the proposed design, and its difference increases as h of the PI film increases. The variables h as well as w affect Δf_{res} by changing a portion of EI_{bare} in the entire cantilever, and it is difficult to derive an uncomplicated expression for Δf_{res} with respect to all the PI film-related parameters. To observe the effects of w and h on the stiffness and Δf_{res} of the PIF-FC, we implement finite element analysis (FEA) using ANSYS software. The stiffness of a fiber cantilever is proportional to the flexural rigidity as $\kappa = 3EI/L_{fc}^3$.

Fig. 4(a) shows the FEA results for the stiffness of the PIF-FC along the x- and y-axes (κ_x and κ_y). There are no significant changes in κ_x because of the small thickness of the PI film; in other words, EI_x has almost the same value as EI_{bare}. On the contrary, κ_y rapidly increases as w and h increase. The contour lines of the stiffness ratio, $\kappa r (= \kappa_y / \kappa_x)$, are depicted on the graphs. If κr is too large, driving voltages with large differences

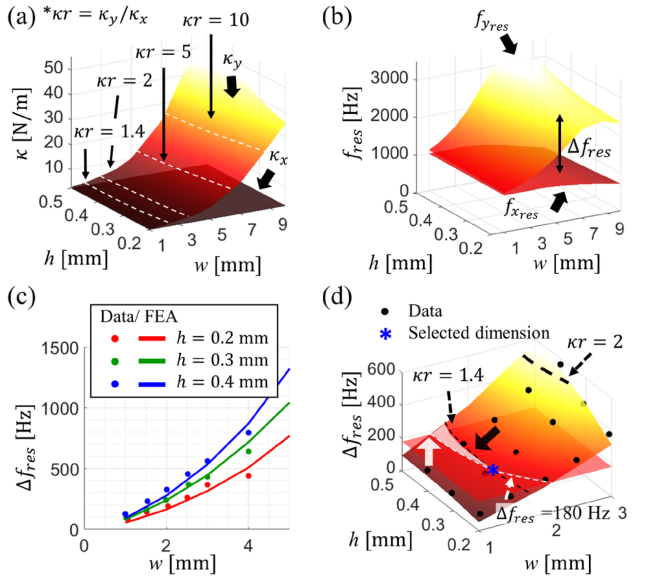

Fig. 4. (a) and (b) FEA results of stiffnesses and resonant frequencies of PIF-FC along both scanning axes. (c) Comparison between FEA and experimental results. (d) FEA results of both frequency separation and contour of the stiffness ratio as well as experimental data.

must be applied to produce similar deflections along the two scanning axes. This can require extremely high voltages over the allowed limits. Fig. 4(b) shows the resonant frequency, f_{res} , of each scanning axis, namely $f_{x_{res}}$ and $f_{y_{res}}$. Here, $f_{x_{res}}$ does not change much with respect to h; however, it gradually decreases as w increases. As the PI film approaches the fiber tip, it works more like a mass, which reduces f_{res}. The value of $f_{y_{res}}$ increases as both w and h increase; however, this value also decreases beyond $w = 7$ mm. To validate the FEA results, the Δf_{res} values of eighteen PIF-FCs having different w and h values are measured, as shown in Fig. 4(c). The FEA results are observed to be in good agreement with the actual data, especially for small values of w below 2.5 mm. Based on the FEA and experimental results, the optimal dimensions of the PI film are selected to ensure that Δf_{res} is greater than 180 Hz and κr is less than 1.4, as indicated by the bold white and dark arrows in Fig. 4(d), respectively. According to these criteria, the dimensions of the PI film were chosen from the white-colored area on the graph; the minimum value of h in this area is chosen, as indicated by the blue-colored asterisk, to reduce the total height of the PIF-FC. Hence, $h = 0.35$ mm and w = 1.7 mm are determined to be the optimal dimensions of the PI film.

Fig. 5(a) shows the frequency responses of the deflections of the PIF-FC at several voltage amplitudes. The maximum deflections along the x- and y-axes are 550 μm and 470 μm at driving frequencies of 1053.5 Hz and 1248.5 Hz, respectively; the Δf_{res} of 195 Hz is enough to eliminate the parasitic resonance and enables the production of clear linear scan patterns, as shown in the inset images between the two graphs. The gray dotted lines indicate the cutoff frequencies, which are decided as the frequencies at which the deflections decrease by $> 15\%$ from the maximum values in this study. The cutoff frequencies are

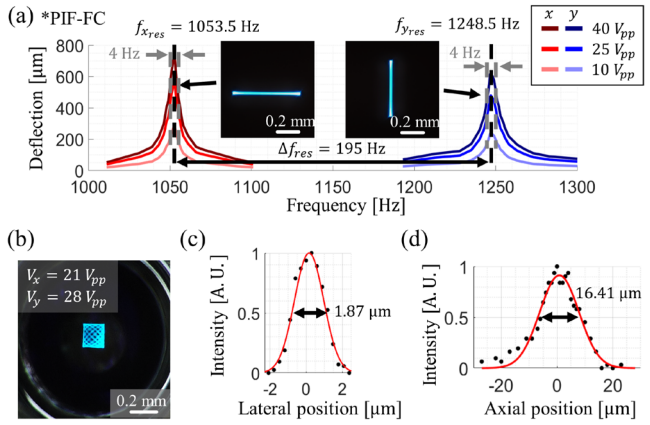

Fig. 5. (a) Frequency responses of the manufactured PIF-FC. (b) Lissajous scanning image after passing through the objective lens. (c) and (d) Measured lateral and axial resolutions of the implemented confocal system, respectively.

used as the upper and lower boundaries in the frequency analysis, which will be explained further in Section III. At the resonant frequency, signals of amplitudes 21 V_{pp} and 28 V_{pp} are applied to the x- and y-axes, respectively, creating a square scan area. This produces a Lissajous pattern having 180 μm × 180 μm FOV after passing through the objective lens, as shown in Fig. 5(b). Fig. 5(c) and (d) is the measured lateral and axial resolutions of 1.87 μm and 16.41 μm, respectively. The objective lens is customized to have a working distance of 60 μm in water and a magnification of 2.87.

III. Modified Phase-Offset-Driven Method

A. Optimization of the Lissajous Scanning Pattern

To reconstruct an image from the measured PMT signals, it is necessary to assign the measured intensities to the correct pixels on the image. As shown in Fig. 6(a), three types of waveforms are considered for this purpose, namely driving, actual, and mapping waveforms, which are represented by the solid black-, red-, and blue-colored lines, respectively. The dotted lines indicate the waveforms at zero driving phases. The graphs along the left side are on the phase axis, and the graphs along the right side are on the time index axis. First, the driving waveforms (X_{driv}, Y_{driv}) have driving frequencies f_x and f_y and phases $\varphi_{x_{driv}}$ and $\varphi_{y_{driv}}$, respectively. The driving phase offset is denoted as $\Delta\varphi_{driv}$ ($\varphi_{x_{driv}} - \varphi_{y_{driv}}$). The actual waveforms (X_{act}, Y_{act}) are used to represent the fiber's movement, and the frequencies of the scanning fiber are assumed to be the same as the driving frequencies. However, the actual phases, $\varphi_{x_{act}}$ and $\varphi_{y_{act}}$, have deviations from the driving signal, i.e., $\Delta\varphi_{x_{act}}$ and $\Delta\varphi_{y_{act}}$, ranging from $-\pi$ to 0 [30], and they can be expressed as follows:

$$\Delta\,\varphi_{i_{act}} = atan\left(\frac{-2\xi_i r_{i_f}}{1-r_{i_f}^2}\right) + n\pi \tag{1}$$

where $n\pi$ is the phase unwrapping component, ξ_i is the damping ratio, and r_{i_f} is the ratio between the driving and resonant frequencies; $r_{i_f} = f_i\,/f_{i_{res}}$. It is necessary to know the actual

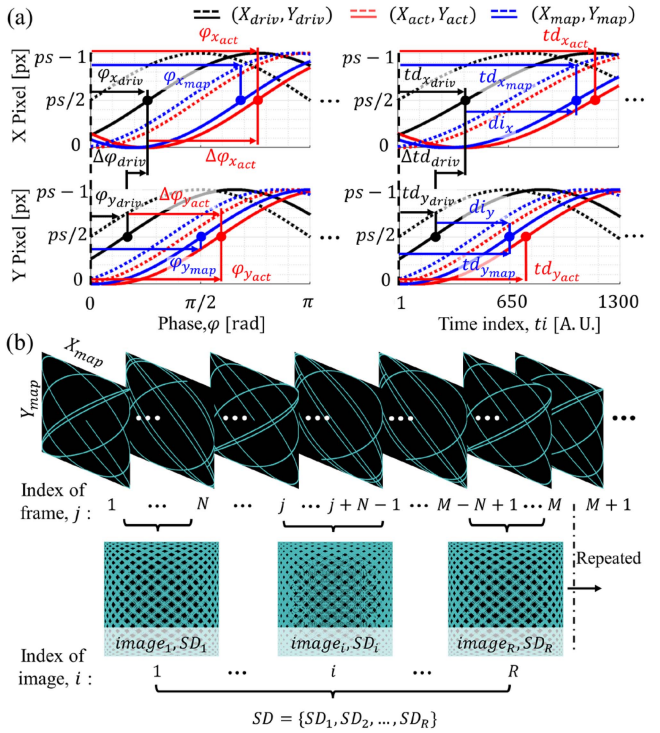

Fig. 6. (a) Parameters of three types of waveforms for image generation: driving, mapping, and actual. (b) Schematic of image reconstruction during Lissajous scanning.

phase lags to reconstruct the correct image without distortion. For image matching, the mapping waveforms, (X_{map}, Y_{map}) should be identical to (X_{act}, Y_{act}). To identify the actual phase without a sensor, a software-based phase calibration can be applied by adjusting the mapping phases $\varphi_{x_{map}}$ and $\varphi_{y_{map}}$ until the interlaced features on the acquired image are eliminated [29], [33]. Here, the driving and mapping waveforms are generated along with a discrete time index, $ti \in \{12, \ldots, 10 \times SN\}$, where SN is the total number of the samples in 1 s and is equal to 3.2×10^6. The driving waveforms can be expressed as follows:

$$\begin{bmatrix} X_{driv}\,(ti) \\ Y_{driv}\,(ti) \end{bmatrix} = \frac{(ps-1)}{2} \begin{bmatrix} sin\,(2\pi f_x T\,(ti - td_{x_{driv}}))) + 1 \\ sin\,(2\pi f_y T\,(ti - td_{y_{driv}}))) + 1 \end{bmatrix} \tag{2}$$

where ps is the number of pixels determined as 352, td is the controllable time delay from the software, and T is the time array; $T = \{\frac{ti}{SN} | ti \in \{12, \ldots, 10 \times SN\}\}$. Therefore, T contains the sampled times of 10 s so that the waveform with frequencies up to one decimal place can be repeated. The mapping waveform is then generated by shifting the sampled time index with the controllable delay indexes di_x and di_y; $X_{map}\,(ti) = X_{driv}\,(ti - di_x)$ and $Y_{map}\,(ti) = Y_{driv}\,(ti - di_y)$. The di_x and di_y can be changed during imaging to modulate the mapping time delays, $td_{x_{map}}$ and $td_{y_{map}}$, which can be expressed by $td_{x_{driv}} + di_x$ and $td_{y_{driv}} + di_y$, respectively. Each time delay can then be converted to phase as follows: $\varphi_x = \frac{2\pi f_x}{SN}\,td_x$ and $\varphi_y = \frac{2\pi f_y}{SN}\,td_y$. Changing the delay indexes by one has the effect of adjusting $\varphi_{x_{map}}$ and $\varphi_{y_{map}}$ by 0.118° and 0.140°, respectively, at the driving frequencies

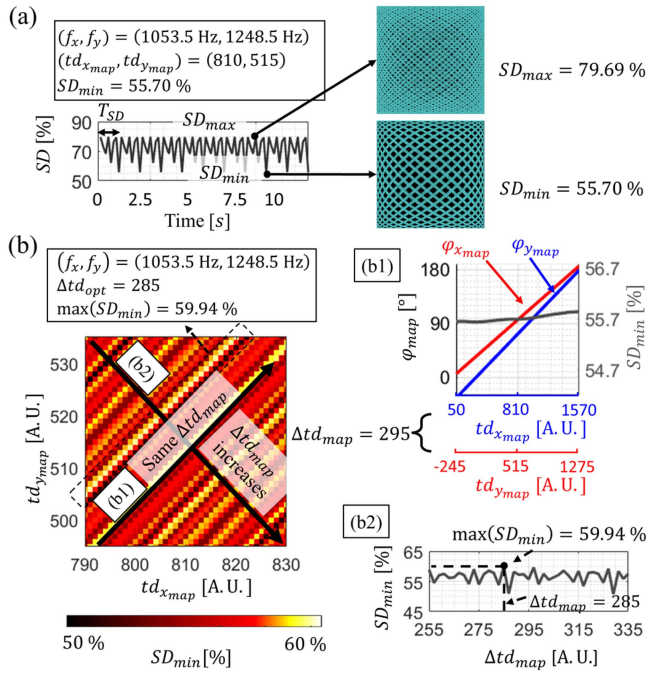

Fig. 7. (a) Simulated result of SD at $(f_x, f_y) = (1053.5\text{ Hz}, 1248.5\text{ Hz})$ and $(di_x, di_y) = (810, 515)$. (b) Time delay analysis to find the maximum value of SD_{min} at a given frequency combination. (b1) Results of the mapping phases and SD_{min} at different time-delays with the constant difference. (b2) Result of SD_{min} at different time-delay differences.

around $(1053.5\text{ Hz},\ 1248.5\text{ Hz})$. Therefore, the di_x and di_y are used to match the mapping time delays with the actual time delays, $td_{x_{act}}$ and $td_{y_{act}}$.

In terms of image reconstruction, the upper image in Fig. 6(b) shows a series of patterns for each frame during the Lissajous scans; j indicates the index of each frame, and M denotes the frame index for the 10 s period. In this study, each frame is obtained at a rate of 320 Hz such that M is 3200. Each image is acquired by accumulating several frames until the image has sufficient SD. Here, i indicates the index of an image, and the imaging speed can be controlled by the frame accumulation number, N. In addition, R represents the image index at the 10 s period for which the imaging patterns are repeated and is defined as M divided by N. The SD is calculated by dividing the number of sampled data points by the total number of pixels. Thus, a high SD can be obtained by increasing N, but there is a tradeoff relationship between the imaging speed and SD. The imaging speed is fixed at 8 Hz by setting N as 40. Then, R becomes 80, and the scan patterns are repeated every 80 images. Each image has a different SD_i, with respect to the image index i. As the scan patterns are repeated every 80 images, so is the SD. SD is an array that includes all possible SD_is during the one period, i.e., $SD = \{SD_i | i \in \{12, \ldots, R\}\}$.

An example SD for one period is shown in Fig. 7(a); these results are obtained from MATLAB simulations, with $(f_x,\ f_y)$ set to $(1053.5\text{ Hz},\ 1248.5\text{ Hz})$ and driving phases set to all zeros, such that $td_{x_{map}}$ and $td_{y_{map}}$ are identical to di_x and di_y. In addition, $td_{x_{map}}$ and $td_{y_{map}}$ are 810 and 515, where $\varphi_{x_{map}}$ and $\varphi_{y_{map}}$ correspond to 96.00° and 72.33°, respectively. Each delay index is experimentally determined to eliminate duplicated artifacts on the acquired images at $(1053.5\text{ Hz},\ 1248.5\text{ Hz})$. The SD has large fluctuations with maximum and minimum values (SD_{max} and SD_{min}) of 79.69% and 55.70%, respectively. It can be clearly seen that a maximal number of pixels are unsampled at the minimum SD. We found that SD graphs obtained by the frequencies with one decimal place have a period, T_{SD} as follows:

$$T_{SD} = \frac{5}{GCF\left(GCF\left(10 \times f_x, 10 \times f_y\right), R/2\right)} \tag{3}$$

where $GCF(a, b)$ is the integer greatest-common-factor of a and b. The detailed derivation on (3) can be found in the supplementary material. In case of $(1053.5\text{ Hz},\ 1248.5\text{ Hz})$, T_{SD} is 1 s and well-fitted with the simulation result. The calculation of T_{SD} thus enables finding the SD_{min} by calculating the SD for one period, which can reduce the analysis time.

To analyze the tendency of SD_{min} with respect to the combinations of time delays, SD_{min} is analyzed by modulating both $td_{x_{map}}$ and $td_{y_{map}}$ by ±20, as shown in Fig. 7(b). The black arrow pointing towards the upper right corner, (b1), represents the combinations in which Δtd_{map} $(td_{x_{map}} - td_{y_{map}})$ is the same constant. The graph (b1) is the result of the mapping phases and SD_{min} at time delays of ±760 from their central values (810 and 515) to analyze the mapping phases of 0° to 180°, and Δtd_{map} at this time has a constant value of 295. The red- and blue-colored lines indicate $\varphi_{x_{map}}$ and $\varphi_{y_{map}}$, respectively. Since the intervals of $\varphi_{x_{map}}$ and $\varphi_{y_{map}}$ have a ratio of $f_x : f_y$, the mapping phase difference changes with respect to the mapping time delay. In contrast, SD_{min} has approximately constant values with respect to the mapping time delay and changes less than 0.2%, as indicated by the gray-colored line. Thus, it is possible to assume that SD_{min} is dependent on Δtd and not the individual values $td_{x_{map}}$ and $td_{y_{map}}$. As shown in Fig. 7(b2), there exists an optimal Δtd_{map}, Δtd_{opt}, that produces the largest value for SD_{min} in a given frequency combination. Finding the Δtd_{opt} by modulating the delay indexes is called "time-delay analysis" in this study. In addition, the calculation of SD_{min} by changing the frequency combination is called "frequency analysis", and each frequency analysis is performed with the time-delay analysis to obtain the maximum value of SD_{min} for a given frequency combination. At $(1053.5\text{ Hz},\ 1248.5\text{ Hz})$, the maximum value of SD_{min} is 59.94%, with a Δtd of 285.

To observe the effects of time-delay analysis, max(SD_{min}) is first analyzed at integer-frequency combinations within the 5 Hz bandwidth without time-delay analysis [see Fig. 8(a)] and with time-delay analysis [see Fig. 8(b)]. The color bar indicates the value of max(SD_{min}) from 0% to 100%, and the time-delay analysis allows finding the maximum value of SD_{min} within a given range of the time delay index, i.e., ±20 from the central values. As shown in Fig. 8(d), there is only one desired frequency combination that produces an SD > 80% without phase analysis; the SD of 80.31% at $(1055\text{ Hz},\ 1250\text{ Hz})$. However, an additional combination is observed to have an SD of 81.52% at $(1054\text{ Hz},\ 1250\text{ Hz})$, with Δtd_{opt} of 357, as seen in Fig. 8(e). However, these integer frequency combinations deviate from the

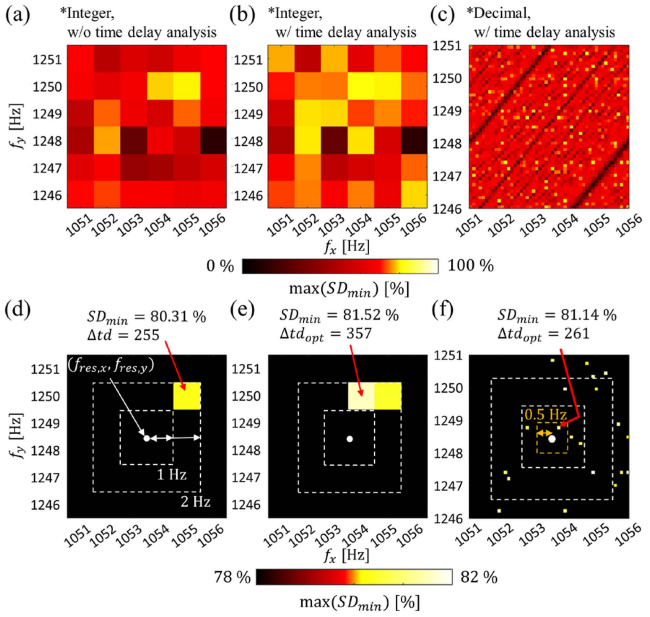

Fig. 8. Simulated results of the frequency analysis at integer frequency combinations (a) without and (b) with time-delay analysis, and (c) decimal frequency combinations with time-delay analysis; (d)–(f) Only the desired combinations allowing SD $> 80\%$.

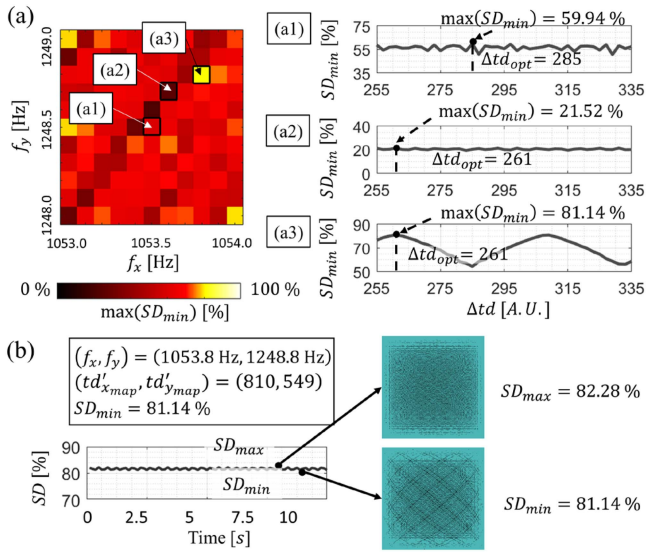

Fig. 9. (a) Simulated results of the max(SD_{min}) for decimal frequency combinations with time-delay analysis within ± 0.5 Hz from the resonant frequencies. (b) SD results of the optimized frequency combinations and time-delay difference.

resonant frequency by up to 1.5 Hz, as indicated by the white dotted boxes. The frequency deviation of 1.5 Hz yields a maximum deflection loss of ~ 60 μm in the implemented PIF-FC. For a more precise analysis, the simulation is performed with decimal frequency combinations with the time-delay analysis, as shown in Fig. 8(c). As the amount of analyzed data increases by 100 times, the analysis can be performed with more cases, and tendencies that were not observed in integer combinations were also visible; the SD tends to be significantly low at frequency differences of 192 Hz and 197 Hz, as shown by the two diagonal dark lines in Fig. 8(c). The decimal frequency analysis also enables finding the twenty desired combinations; four of which are within a 1 Hz boundary and one has only 0.3 Hz deviation from the resonant frequency, with SD of 81.14% and Δdi_{opt} of 261 as shown in Fig. 8(f).

The frequency analysis result within ± 0.5 Hz from the resonant frequencies is shown in Fig. 9(a); three points are designated on the graph as (a1), (a2), and (a3), which correspond to the three frequency combinations (1053.5 Hz, 1248.5 Hz), (1053.6 Hz, 1248.7 Hz), and (1053.8 Hz, 1248.8 Hz), respectively. On the right side of Fig. 9(a), the three graphs show the values of SD_{min} with respect to Δtd at each frequency combination. A randomized tendency of SD_{min} is achieved at (a1), resulting in a maximum value of 59.94% for Δtd of 285. The condition (a2) produces a maximum SD_{min} of 21.52% for Δtd of 261, which rarely fills pixels. The best result is achieved at (a3) for a maximum SD_{min} of 81.14% at $\Delta td = 261$. In addition, SD_{min} shows a periodic sawtooth-like tendency. Therefore, SD_{min} gradually decreases if Δtd deviates from the Δtd_{opt}. From this analysis, the best combination of frequencies is determined as (1053.8 Hz, 1248.8 Hz) with the optimized delay index difference of 261. Fig. 9(b) shows the simulated SD result at the optimal combination of frequencies and the time delay difference. $td'_{x_{map}}$ and $td'_{y_{map}}$ are the arbitrary mapping time delays that have a difference of Δtd_{opt}. For example, if $(td_{x_{map}}, td_{y_{map}}) = (810, 549)$, Δtd is 261, which is the optimal time-delay difference at (1053.8 Hz, 1248.8 Hz) such that $\Delta td_{opt} = 261$. The fluctuations in the SD graph are significantly reduced from that of Fig. 7(a), resulting in maximum and minimum values of 82.28% and 81.14%, respectively. Two representative scanning patterns are shown on the right side of the graph. When SD_i has a maximum value of 82.28%, unsampled pixels are barely observed; even if SD_i has a minimum value of 81.14%, the unsampled pixels are not prominent.

B. Modification on Driving Phase-Offset

Even though the best frequency combination and Δtd_{opt} are found, Δtd_{act} ($td_{x_{act}} - td_{y_{act}}$) is mostly different from Δtd_{opt} as a result of finding the actual phases by adjusting the delay indexes. As shown in Fig. 10(a), the actual phases can require the actual delay indexes of $di_{x_{act}}$ and $di_{y_{act}}$ with the deviations Δdi_x and Δdi_y from the desired values di'_x and di'_y. Here, $di'_x - di'_y$ has Δtd_{opt}, and the difference of the deviations ($\Delta di_x - \Delta di_y$) is denoted as Δdi_{dev}. Therefore, Δtd_{act} can be expressed as $\Delta td_{opt} + \Delta di_{dev}$. The graph in Fig. 10(a) is a simulated SD result when $\varphi_{x_{driv}}$ and $\varphi_{y_{driv}}$ are all-zeros, and Δdi_x and Δdi_y are $+10$ and -10, respectively, which results in a Δdi_{dev} of $+20$. This deviation makes Δtd_{act} different from Δtd_{opt}, causing the minimum SD to decrease from 81.14% to 58.49%.

To solve this problem, we applied the modified phase-offset to the driving voltages, as shown in Fig. 10(b). The graph in Fig. 10(b) is the simulated result when the modified driving phase-offset, $\Delta\varphi_{driv}$, is applied. For simplicity, $\varphi_{y_{driv}}$ is kept to zero, and $\varphi_{x_{driv}}$ of $\Delta\varphi_{driv}$ is applied. Δdi_{act} is then calculated by $di_{x_{act}} - di_{y_{act}}$, which are found by image matching. Δdi_{dev}

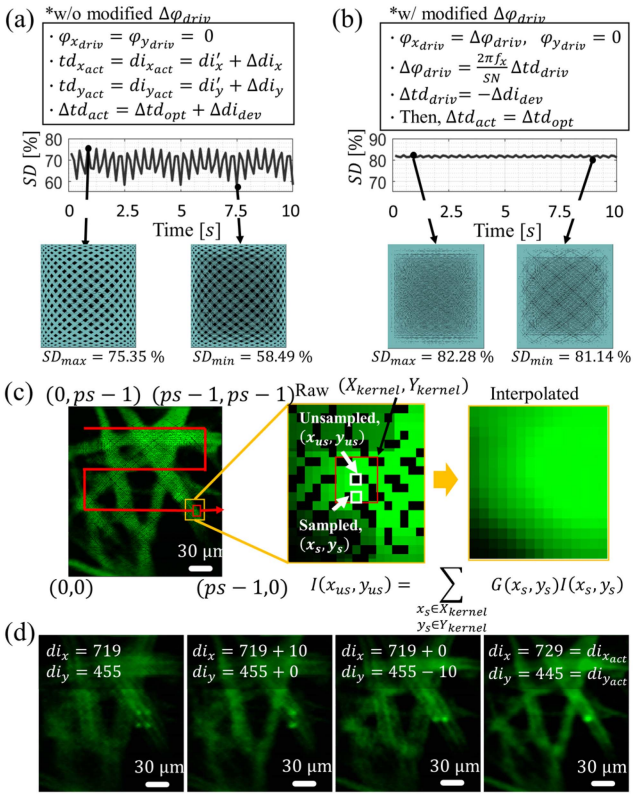

Fig. 10. (a) SD graph when the actual phases are different from the optimized values. (b) SD graph when the modified driving phase offset is applied. (c) Gaussian interpolation. (d) Image matching by modulating the mapping phases.

can be achieved by subtracting Δtd_{opt} from Δdi_{act}. In the previous case where both driving phases are all-zeros, Δtd_{act} is the same with Δdi_{act} which has a deviation of Δdi_{dev} from Δtd_{opt}. To compensate for Δdi_{dev}, Δtd_{driv} of $-\Delta di_{dev}$ is finally applied to subtract Δdi_{dev}, allowing td_{act} to be the same with td_{opt}; thus, the driving phases $(\varphi_{x_{driv}}, \varphi_{y_{driv}})$ of $(\Delta\varphi_{driv}, 0\,^\circ)$ with $\Delta\,\varphi_{driv} = -\frac{2\pi f_x}{SN}\Delta di_{dev}$ can be used as a modified driving phase-offset. For Δdi_{dev} of $+20$, $\Delta\varphi_{driv}$ of $-2.37\,^\circ$ is applied, and the scan patterns return to their optimized states with a minimal SD of 81.14%. This means that any values of the delay indexes can obtain the optimized scanning pattern because the Δdi_{dev} can be compensated by modulating the driving phase-offset.

Even though the scanning pattern is optimized, there are still inevitable unsampled blank pixels, as shown in Fig. 10(c), which depicts the image of a lens-cleaning tissue soaked with fluorescein. The origin of the image coordinates is located at the bottom left, and the unsampled pixel coordinates are each found whenever an image is acquired. As shown in the detailed image within the yellow box, there are both unsampled and sampled data pixels, which are denoted as $(x_{us},\ y_{us})$ and $(x_s,\ y_s)$, respectively. To determine the intensities at the unsampled pixels, a natural neighborhood interpolation method using a normalized Gaussian weight is applied [20], [38]. The natural neighborhood interpolation is a fast and simple method [20], and the Gaussian weights are applied to achieve a denoised and reliable interpolated image [38]. $I(x_{us},\ y_{us})$ represents the intensities at the unsampled pixels, $(x_{us},\ y_{us})$, and $I(x_s,\ y_s)$ represents the intensities at the sampled pixels, $(x_s,\ y_s)$. Here, the normalized Gaussian kernel, $G(x_s, y_s)$ has a size of 5×5 pixels as shown in the red-colored box. X_{kernel} and Y_{kernel} are the sets of x and y coordinates within the kernel, respectively. The total number of sampled pixels varies from one kernel to another, so the normalization of $G(x_s, y_s)$ is performed for each kernel. Then, the weighted sum of the neighboring sampled intensities could produce smooth interpolated results, as shown in the right side of Fig. 10(c).

After interpolation, it is easier to match the actual phases by observing the monitored image with enhanced quality. For image matching, we roughly chose the initial delay indexes using a graphical user interface and coarsely changed the values until the acquired image was almost merged as shown in the leftmost image of Fig. 10(d). The replicated features of a lens-cleaning tissue can be observed along both scan axes, for di_x and di_y of 719 and 455, respectively. If di_x is modulated from 719 to 729, the interlaced images are merged along the x-axis. On the other hand, the corrections can be applied along the y-axis when di_y is varied from 455 to 445. As shown in the rightmost panel of Fig. 10(d), an accurate image of the lens-cleaning tissue can be obtained at di_x of 729 and di_y of 445, respectively. The mapping delay indexes now can represent the actual delay indexes $di_{x_{act}}$ and $di_{y_{act}}$. In this study, this adjustment refers to the phase calibration step that helps find the actual phases.

However, Δtd_{act} has a deviation from the optimal value. If both driving phases are all zeros, Δtd_{act} is 284 in case that $(di_{x_{act}},\ di_{y_{act}})$ is (729, 445); because $(td_{x_{act}},\ td_{y_{act}})$ is identical to $(di_{x_{act}}, di_{y_{act}})$. Δtd_{act} of 284 deviates from Δtd_{opt} by 23 such that $\Delta\ di_{dev} = 23$. To compensate for the deviation of 23, $\Delta\varphi_{driv}$ of $-2.73\,^\circ$ can be calculated by the presented driving phase-offset modification. As a result, $(\varphi_{x_{driv}},\ \varphi_{y_{driv}})$ of $(-2.73\,^\circ, 0\,^\circ)$ can be applied to shift the time index of X_{map} for 23 in the negative direction. Then, Δtd_{act} becomes 261, which is the same with the optimal value.

Here, we fixed the $\Delta\varphi_{driv}$ after the first phase calibration is completed. In addition, the image matching is performed manually during imaging to compensate for the variations in the actual phases. To see the effect of the variations in the actual delay indexes on the SD, both delay indexes and SD were recorded for 20 min while performing the image matching of the lens-cleaning tissue. The red and blue lines in Fig. 11(a) are the recorded values of di_x and di_y with the initial values of 729 and 445, respectively. The delay indexes were modified whenever image distortions occurred, and the black dotted-line in Fig. 11(b) indicates the corresponding actual delay index difference, Δdi_{act}. The initial Δdi_{act} is 284 which has Δdi_{dev} of 23 from the Δtd_{opt} (green dotted-line). The $\Delta\varphi_{driv}$ of -2.73° enables to reduce Δtd_{act} (black rigid-line) by 23 as indicated by the black rigid arrow. The maximal and minimal Δtd_{act} are 263 and 257, respectively; Δtd_{dev} ranges from -4 to 2. Fig. 11(c) shows the recorded SDs during image acquisition without and with a modified driving phase-offset, which are

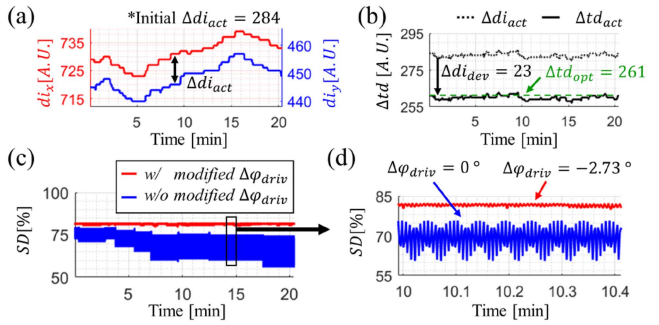

Fig. 11. (a) Graph of mapping phases during the 20 min image acquisition. (b) Magnified graph of the mapping phase difference and optimal phase difference. (c) Measured SDs without and with modification on the driving phase-offsets. (d) Magnified graph from the interval of 10 to 10.4 min.

represented by the blue and red lines, respectively. The former is achieved when the applied driving phases are zeros; thus, it does not consider the Δtd_{dev} ranging from 19 to 25. There are large fluctuations in the SD from 60% to 75%, as can be seen in the blue line in the magnified graph in Fig. 11(d). On the contrary, the red line is acquired by applying a driving phase-offset of $-2.73°$, which is calculated by using the initial Δdi_{dev} of 23. The recorded minimum SD was 79.26% when the mapping phases were changed excessively, and an SD of 80% or more was obtained in most cases, as expected from the simulation results in Fig. 10(b)

IV. Results and Discussion

The USAF 1951 test pattern and several plants were imaged to show the capability of the proposed confocal imaging, with the imaging speed of 8 Hz (see Video S1). Fig. 12(a) shows the stitched image that includes patterns from groups 6 and 7 on the USAF 1951 test chart. The line pairs and their numberings are observed to be well distinguished. Plants are generally good candidates for fluorescent imaging as their microstructures can be observed with a simple staining procedure. First, the lower epidermis of *Arabidopsis thaliana* grown for ten days is soaked in fluorescein for 1 min to stain its cell membrane. In terms of the lower epidermis, the pavement cells and stomatal pores can be observed, and the morphologies of these components are known to have jigsaw-puzzle- and bean-shaped features, respectively [39]. The pavement cells and tiny stomatal pores of $\sim 10\ \mu$m, surrounded by two guard cells, can be visualized well, as shown in Fig. 12(b). Fig. 12(c) is an image of a tulip petal soaked in fluorescein for 1 min; the epidermal cells with elongated features are seen, along with the stomatal pore and guard cells. The size of the stomatal pore of the tulip petal is much larger than that of *A. thaliana* grown for ten days. The shapes, sizes, and densities of the stomatal pores play essential roles in plant research, such as physiological petal movements and the investigation of signaling pathways [40]. Fig. 12(d) is an image of the epidermis of an onion peel. It was stained by dipping in fluorescein for 1 min. The epidermis of the onion peel has stacked rectangular-shaped cells with prominent nuclei, and the cell structure can be visualized well.

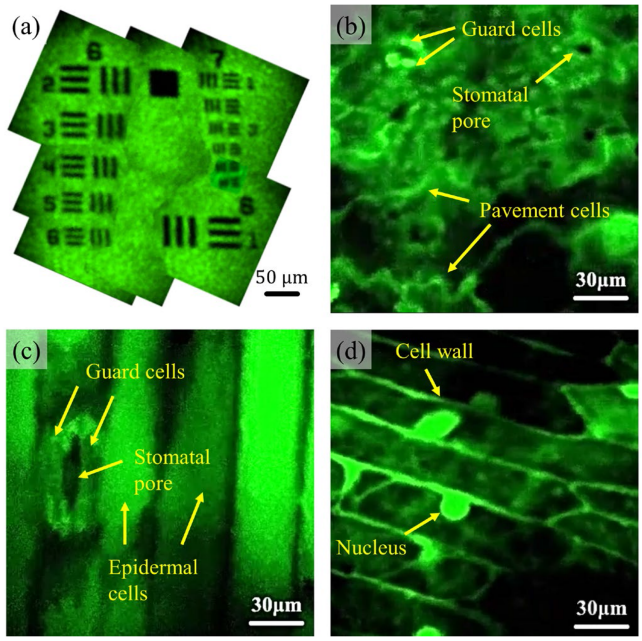

Fig. 12. Confocal images of the USAF 1951 test chart and several plants (see Video S1). (a) Stitched image of the patterns in groups 6 and 7 on the USAF 1951 test chart. (b) and (c) Lower epidermis of the *Arabidopsis thaliana* leaf and a tulip petal, respectively. (d) Onion peel epidermal cells.

The gastrointestinal tract was extracted from a Sprague Dawley rat grown for ten weeks as an animal sample. A 2% solution of isoflurane (O_2 100%) was used as a respiratory anesthetic. A fluorescein solution of 1 mL (20 mg/mL) was introduced by intravenous tail injection. The entire surgical procedure followed the experimental protocol approved by the Animal Experiment Ethics Committee of Daegu Gyeongbuk Institute of Science and Technology (approval no. DGIST-IACUC-21042801-0001) with every effort to alleviate the subject's pain. The gastrointestinal tract comprises several digestive organs from the mouth to the anus, and ex-vivo images were acquired sequentially from the esophagus to the colon at a rate of 8 Hz (see Video S2). Fig. 13(a) depicts the image of the esophagus; several squamous cells and clear spaces can be visualized well [41]. Fig. 13(b) shows the corpus of the stomach; the gastric pits in the corpus generally have roundish shapes, and this feature can be observed [42]. The duodenal gland has a round pit in the middle, as seen in Fig. 13(c), and the goblet cells can be recognized with their black dots, as indicated by the yellow arrows. The colon images are shown in Fig. 13(d); the patterns of the crypt lumen can be identified from their known morphologies [43]. The ability to image tissue morphology, such as the gastric and intestinal glands, can provide important clues for diagnosing intestinal metaplasia or cancer.

V. Conclusion

In this study, the Lissajous scanning system was implemented using a commercial thin PI film-based frequency separator. In addition, the modified phase-offset-driven method was proposed to maintain a high SD of $> 80\%$ at the imaging speed of 8 Hz.

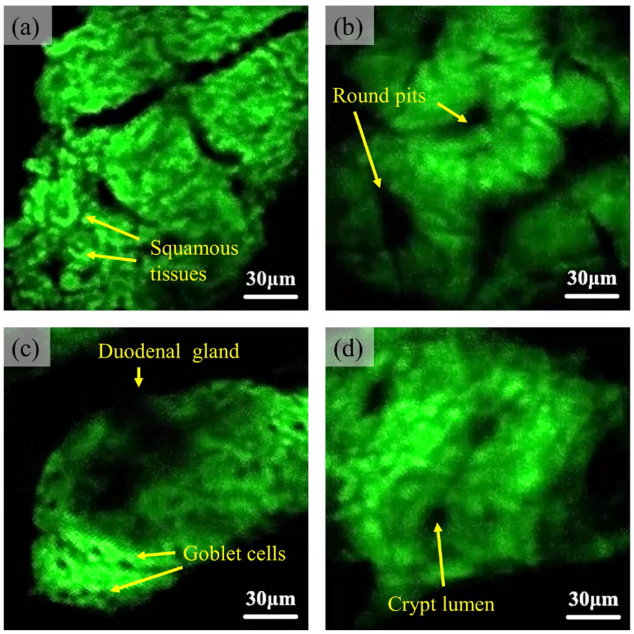

Fig. 13. Confocal images of the GI tract of an SD rat (see Video S2). (a) Esophagus. (b) Corpus of the stomach. (c) Duodenum. (d) Colon.

The PI film is a good candidate for a frequency separator in a resonant fiber scanning system owing to its low cost, compactness, dimensional flexibility, and stability. The results from FEA and experiments were used to determine the width and height of the optimized PI film as 1.7 mm and 0.35 mm, respectively. The PIF-FC developed herein could be resonated with the lever mechanism and had a sufficient frequency separation of 195 Hz. In addition, 180 μm $\times$ 180 μm FOV is achieved with signals of amplitudes 21 V_{pp} and 28 V_{pp} along the x- and y-axes, respectively.

To find the optimal combination of decimal frequencies and time delay difference, the SD_{min} was analyzed by both the frequency and time-delay analysis. In addition, the modified driving phase offset could be applied to the driving voltages to compensate for the actual phase shift. These methods of finding and maintaining the optimal nonrepeating Lissajous pattern are particularly beneficial for a system with a high Q-factor, which may be difficult to achieve with an optimized combination of integer frequencies in terms of high SD and imaging speed. The images were acquired from the USAF 1951 test chart, several plants, and different parts of a rat gastrointestinal tract to demonstrate the ability of the system to visualize microstructures.

In future works, automatic modulations of the mapping delay indexes and driving phase offset can be considered. The proposed system requires manual changes to the mapping delay indexes at this time to correct the acquired images, and the driving phase is maintained constant after phase calibration. For automatic image matching, the sharpness of the image can be calculated and used to continuously modulate the mapping phases [29], [33]. At the same time, the modified driving phase offset can be applied to preserve the optimal pattern in real-time. A phase-locked-loop-based control scheme or additional circuitry can be implemented to deliberately change the $\Delta\varphi_{driv}$ during scanning. It means that both image matching and optimized scan patterns can be automatically achieved. This method may be applied to all Lissajous scanning systems, enabling the continuous acquisition of high SDs with good imaging speeds.

Acknowledgment

The authors would like to thank J. Kim for providing 10 DAG (days after germination) *Arabidopsis thaliana* plants.

References

[1] M. Kim, C. Park, S. Je, H. Jang, C. Joo, and S. Kang, "Real-time compensation of simultaneous errors induced by optical phase difference and substrate motion in scanning beam laser interference lithography system," *IEEE/ASME Trans. Mechatronics*, vol. 23, no. 4, pp. 1491–1500, Aug. 2018.

[2] L. Li, J. Huang, S. S. Aphale, and L. Zhu, "A smoothed raster scanning trajectory based on acceleration-continuous B-spline transition for high-speed atomic force microscopy," *IEEE/ASME Trans. Mechatronics*, vol. 26, no. 1, pp. 24–32, Feb. 2021.

[3] P. Cheng and C. H. Menq, "Visual tracking of six-axis motion rendering ultraprecise visual servoing of microscopic objects," *IEEE/ASME Trans. Mechatronics*, vol. 23, no. 4, pp. 1564–1572, Aug. 2018.

[4] W. Gao *et al.*, "Precise automated intracellular delivery using a robotic cell microscope system with three-dimensional image reconstruction information," *IEEE/ASME Trans. Mechatronics*, vol. 25, no. 6, pp. 2870–2881, May 2020.

[5] B. Tayebi, W. Kim, B. J. Yoon, and J. H. Han, "Real-time triple field of view interferometry for scan-free monitoring of multiple objects," *IEEE/ASME Trans. Mechatronics*, vol. 23, no. 1, pp. 160–166, Jan. 2017.

[6] A. Kazemipour *et al.*, "Kilohertz frame-rate two-photon tomography," *Nat. Methods*, vol. 16, no. 8, pp. 778–786, Aug. 2019.

[7] Z. Sun *et al.*, "Task space motion control for AFM-based nanorobot using optimal and ultralimit archimedean spiral local scan," *IEEE Robot. Autom. Lett.*, vol. 5, no. 2, pp. 282–289, Apr. 2020.

[8] N. Nikooienejad, A. Alipour, M. Maroufi, and S. R. Moheimani, "Video-rate non-raster AFM imaging with cycloid trajectory," *IEEE Trans. Control Syst. Technol.*, vol. 28, no. 2, pp. 436–447, Dec. 2018.

[9] H. Pahlevaninezhad *et al.*, "Nano-optic endoscope for high-resolution optical coherence tomography in vivo," *Nat. Photon.*, vol. 12, no. 9, pp. 540–547, Sep. 2018.

[10] W. Liang *et al.*, "Throughput-speed product augmentation for scanning fiber-optic two-photon endomicroscopy," *IEEE Trans. Med. Imag.*, vol. 39, no. 12, pp. 3779–3787, Jun. 2020.

[11] K. Liang *et al.*, "Cycloid scanning for wide field optical coherence tomography endomicroscopy and angiography in vivo," *Optica*, vol. 5, no. 1, pp. 36–43, Jan. 2018.

[12] E. J. Seibel *et al.*, "Tethered capsule endoscopy, a low-cost and high-performance alternative technology for the screening of esophageal cancer and Barrett's esophagus," *IEEE Trans. Biomed. Eng.*, vol. 55, no. 3, pp. 1032–1042, Feb. 2008.

[13] W. Liang, G. Hall, B. Messerschmidt, M. J. Li, and X. Li, "Nonlinear optical endomicroscopy for label-free functional histology in vivo," *Light Sci. Appl.*, vol. 6, no. 11, pp. e17082–e17082, Nov. 2017.

[14] D. Do, H. Yoo, and D. G. Gweon, "Fiber-optic raster scanning two-photon endomicroscope using a tubular piezoelectric actuator," *J. Biomed. Opt.*, vol. 19, no. 6, Jun. 2014, Art. no. 066010.

[15] J. Sawinski and W. Denk, "Miniature random-access fiber scanner for in vivo multiphoton imaging," *J. Appl. Phys.*, vol. 102, no. 3, Jun. 2007, Art. no. 034701.

[16] K. Hwang *et al.*, "Handheld endomicroscope using a fiber-optic harmonograph enables real-time and in vivo confocal imaging of living cell morphology and capillary perfusion," *Microsyst. Nanoeng.*, vol. 6, no. 1, pp. 1–11, Sep. 2020.

[17] R. Khayatzadeh, O. Ferhanoğlu, and F. Çivitci, "Unwarped lissajous scanning with polarization maintaining fibers," *IEEE Photon. Technol. Lett.*, vol. 29, no. 19, pp. 1623–1626, Oct. 2017.

[18] W. Liang, K. Murari, Y. Y. Zhang, Y. Chen, X. D. Li, and M. J. Li, "Increased illumination uniformity and reduced photodamage offered by the lissajous scanning in fiber-optic two-photon endomicroscopy," *J. Biomed. Opt.*, vol. 17, no. 2, Feb. 2012, Art. no. 021108.

[19] Y. H. Seo, K. Hwang, H. Kim, and K. H. Jeong, "Scanning MEMS mirror for high definition and high frame rate lissajous patterns," *Micromachines*, vol. 10, no. 1, Jan. 2019, Art. no. 67.
[20] Q. A. Tanguy *et al.*, "Real-time lissajous imaging with a low-voltage 2-axis MEMS scanner based on electrothermal actuation," *Opt. Exp.*, vol. 28, no. 6, pp. 8512–8527, Mar. 2020.
[21] J. Wang, G. Zhang, and Z. You, "Design rules for dense and rapid lissajous scanning," *Microsyst. Nanoeng.*, vol. 6, no. 1, pp. 1–7, Nov. 2020.
[22] D. Brunner, H. W. Yoo, R. Schroedter, and G. Schitter, "Adaptive lissajous scanning pattern design by phase modulation," *Opt. Exp.*, vol. 29, no. 18, pp. 27989–28004, Aug. 2021.
[23] N. Zhang *et al.*, "Compact piezoelectric transducer fiber scanning probe for optical coherence tomography," *Opt. Lett.*, vol. 39, no. 2, pp. 186–188, Jan. 2014.
[24] T. Wu, Z. Ding, K. Wang, M. Chen, and C. Wang, "Two-dimensional scanning realized by an asymmetry fiber cantilever driven by single piezo bender actuator for optical coherence tomography," *Opt. Exp.*, vol. 17, no. 16, pp. 13819–13829, Aug. 2009.
[25] S. Moon, S. W. Lee, M. Rubinstein, B. J. Wong, and Z. Chen, "Semi-resonant operation of a fiber-cantilever piezotube scanner for stable optical coherence tomography endoscope imaging," *Opt. Exp.*, vol. 18, no. 20, pp. 21183–21197, Sep. 2010.
[26] A. Bazaei, Y. K. Yong, and S. R. Moheimani, "High-speed Lissajous-scan atomic force microscopy: Scan pattern planning and control design issues," *Rev. Sci. Instrum.*, vol. 83, no. 6, Jun. 2012, Art. no. 063701.
[27] C. L. Hoy, N. J. Durr, and A. Ben-Yakar, "Fast-updating and nonrepeating lissajous image reconstruction method for capturing increased dynamic information," *Appl. Opt.*, vol. 50, no. 16, pp. 2376–2382, May 2011.
[28] S. Z. Sullivan *et al.*, "High frame-rate multichannel beam-scanning microscopy based on lissajous trajectories," *Opt. Exp.*, vol. 22, no. 20, pp. 24224–24234, Oct. 2014.
[29] M. Birla, et al., "Image processing metrics for phase identification of a multi-axis MEMS scanner used in single-pixel imaging," *IEEE/ASME Trans. Mechatronics.*, vol. 26, no. 3, pp. 1445–1454, Jun. 2021.
[30] M. H. H. Mokhtar and R. R. A. Syms, "Resonant fiber scanner with optical feedback," *Opt. Exp.*, vol. 22, no. 21, pp. 25629–25634, Oct. 2014.
[31] Y. Chen *et al.*, "Motion estimation for a compact electrostatic microscanner via shared driving and sensing electrodes in endomicroscopy," *IEEE/ASME Trans. Mechatronics*, vol. 25, no. 2, pp. 661–672, Mar. 2020.
[32] E. Csencsics and G. Schitter, "System design and control of a resonant fast steering mirror for lissajous-based scanning," *IEEE/ASME Trans. Mechatronics*, vol. 22, no. 5, pp. 1963–1972, Jul. 2017.
[33] N. O. Loewke *et al.*, "Software-based phase control, video-rate imaging, and real-time mosaicing with a Lissajous-scanned confocal microscope," *IEEE Trans. Med. Imag.*, vol. 39, no. 4, pp. 1127–1137, Sep. 2019.
[34] Q. T. Nguyen and R. Y. Tsien, "Fluorescence-guided surgery with live molecular navigation—A new cutting edge," *Nat. Rev. Cancer*, vol. 13, no. 9, pp. 653–662, Sep. 2013.
[35] C. Qu, J. Hu, X. Liu, Z. Li, and Y. Ding, "Morphology and mechanical properties of polyimide films: The effects of UV irradiation on microscale surface," *Materials*, vol. 10, no. 11, Nov. 2017, Art. no. 1329.
[36] J. Sawinski and W. Denk, "Miniature random-access fiber scanner for in vivo multiphoton imaging," *J. Appl. Phys.*, vol. 102, no. 3, Jun. 2007, Art. no. 034701.
[37] C. A. Van Eysden and J. E. Sader, "Resonant frequencies of a rectangular cantilever beam immersed in a fluid," *J. Appl. Phys.*, vol. 100, no. 11, Dec. 2006, Art. no. 114916.
[38] M. Niknejad, H. Rabbani, and M. Babaie-Zadeh, "Image restoration using Gaussian mixture models with spatially constrained patch clustering," *IEEE Trans. Image Process.*, vol. 24, no. 11, pp. 3624–3636, Jun. 2015.
[39] P. Qian, S. Hou, and G. Guo, "Molecular mechanisms controlling pavement cell shape in Arabidopsis leaves," *Plant Cell Rep.*, vol. 28, no. 8, pp. 1147–1157, Jun. 2009.
[40] A. K. Azad, Y. Sawa, T. Ishikawa, and H. Shibata, "Temperature-dependent stomatal movement in tulip petals controls water transpiration during flower opening and closing," *Ann. Appl. Biol.*, vol. 150, no. 1, pp. 81–87, Jan. 2007.
[41] T. J. Muldoon, S. Anandasabapathy, D. Maru, and R. Richards-Kortum, "High-resolution imaging in Barrett's esophagus: A novel, low-cost endoscopic microscope," *Gastrointest. Endosc.*, vol. 68, no. 4, pp. 737–744, Oct. 2008.
[42] M. Goetz, "Characterization of lesions in the stomach: Will confocal laser endomicroscopy replace the pathologist?," *Best. Pract. Res. Clin. Gastroenterol.*, vol. 29, no. 4, pp. 589–599, Aug. 2015.
[43] A. L. Polglase, W. J. McLaren, S. A. Skinner, R. Kiesslich, M. F. Neurath, and P. M. Delaney, "A fluorescence confocal endomicroscope for in vivo microscopy of the upper-and the lower-GI tract," *Gastrointest. Endosc.*, vol. 62, no. 5, pp. 686–695, Nov. 2005.

Jintaek Im received the B.S. degree from the School of Basic Science in 2018, and is currently working toward the Integrated M.S. with Ph.D. degree with the Department of Robotics and Mechatronics Engineering, the Daegu Gyeonbuk Institute of Science and Technology, Daegu, South Korea.

His research interests include opto-mechatronics, biomedical device, microscale sensor and actuator, signal processing, and adaptive control.

Yeonhee Chang (Student Member, IEEE) received the B.S. degree in biotechnology and bioinformatics from the Korea University, Seoul, South Korea, in 2015, the M.S. degree in robotics engineering from the Daegu Gyeongbuk Institute of Science and Technology, Daegu, South Korea, in 2018. She is currently working toward the Ph.D. degree with the Department of Robotics and Mechatronics Engineering, Daegu Gyeongbuk Intstitute of Science and Technology, Daegu, South Korea.

Her research interests include biomedical imaging system, opto-mechatronics, precision control, and signal processing.

Cheol Song (Member, IEEE) received the B.S. degree in mechanical engineering from Seogang University, Seoul, South Korea, in 2003 and the M.S. and Ph.D. degrees in mechanical engineering from KAIST, Daejeon, South Korea, in 2006 and 2010, respectively.

From 2011 to 2013, he was a Postdoctoral Researcher with the Department of Electrical and Computer Engineering, Johns Hopkins University. He is currently an Associate Professor of robotics and mechatronics engineering with Daegu Gyeongbuk Institute of Science and Technology. His current research interests include intelligent opto-mechatronics, human robot cooperation, biomedical robotics, and precision actuator and sensor.